Proceedings of the ASME 2026 45th International Conference on Ocean, Offshore and Arctic Engineering
OMAE2026
June 7-12, 2026, Tokyo, Japan

OMAE2026-181871

TRIPPING EFFECTS ON BOUNDARY LAYER TRANSITION IN FLOW OVER AN AXISYMMETRIC BODY OF REVOLUTION

Guoqing Fan[1], Fuchang Zhou[2], Weiwen Zhao[1], Maokun Ye[1], Decheng Wan[1*]

[1] Computational Marine Hydrodynamic Lab (CMHL), School of Ocean and Civil Engineering, Shanghai Jiao Tong University, Shanghai, China
[2] Wuhan Second Ship Design and Research Institute, Wuhan, China
*Corresponding author: dcwan@sjtu.edu.cn

ABSTRACT

In this study, wall-resolved large-eddy simulations (WRLES) are performed for flow over the DARPA SUBOFF bare hull at a Reynolds number of $Re_L = 1.1\times10^6$ to examine the effects of tripping strategies on turbulent boundary-layer development and wall pressure fluctuations. Two turbulence generation approaches are considered: a numerical trip implemented via wall-normal blowing with an amplitude of $0.18U_\infty$, and a circular trip wire with a diameter of 0.0075D. The results indicate that the circular trip wire induces intense but highly localized pressure fluctuations immediately downstream of the trip location, followed by rapid attenuation, suggesting a limited influence on the downstream flow evolution. In contrast, the numerical trip results in a delayed transition, characterized by an extended transitional region and a pronounced overprediction of wall pressure root-mean-square levels over a substantial downstream extent. These findings demonstrate that inappropriate numerical tripping can lead to over-tripping effects and artificial amplification of wall pressure fluctuations. By comparison, the circular trip wire provides a more realistic representation of turbulent transition and near-wall dynamics in high-Reynolds-number axisymmetric boundary layers.

Keywords: Boundary layer transition; DARPA SUBOFF; wall pressure fluctuations; wall-resolved large eddy simulation

1. INTRODUCTION

Wall-bounded turbulent flows over underwater vehicles play a critical role in determining hydrodynamic performance, acoustic signatures, and structural loading. The flow around a submerged body of revolution is inherently complex, involving laminar–turbulent transition in the forebody region, strong adverse pressure gradients toward the aft section, and intricate interactions induced by appendages such as sail, control surfaces, and propulsors. These effects may lead to flow separation, large-scale unsteady structures, and pronounced wall pressure fluctuations, which are closely associated with flow-induced noise and vibration. A detailed understanding of turbulent boundary-layer development and wall pressure characteristics over underwater vehicles is therefore of considerable importance for both fundamental research and engineering applications, including drag prediction, flow control, and low-noise design.

To facilitate systematic investigations of underwater vehicle hydrodynamics, the DARPA SUBOFF model [1] has been widely adopted as a canonical benchmark geometry. Owing to its well-defined axisymmetric hull form and the availability of extensive experimental and numerical data, the SUBOFF bare hull has served as a reference configuration for studies on boundary-layer transition, turbulent flow development, pressure distribution, and wake dynamics. Numerous experimental measurements [2–4] and high-fidelity numerical simulations [5–10] have been conducted on this model across a range of Reynolds numbers, providing valuable insights into the flow physics of axisymmetric underwater vehicles and offering a solid foundation for model validation and methodological assessment.

A key issue in both experimental and numerical studies of model-scale underwater vehicles is the treatment of laminar–turbulent transition in the forebody region. At model-scale Reynolds numbers, the boundary layer over the nose and forward portion of the hull often remains laminar unless artificial disturbances are introduced. In experimental investigations, transition is commonly triggered using physical tripping devices such as circular trip wires mounted near the nose. In numerical simulations, however, if no artificial tripping is applied, large portions of the hull may similarly remain laminar. Various numerical tripping strategies have therefore been proposed, including wall-normal blowing or suction, the introduction of inflow turbulence, and the use of localized geometric perturbations to mimic the effect of experimental trip wires. Zhu et al. [10] systematically investigated the influence of incoming-turbulence intensity on the curved-edge boundary layer over the SUBOFF bow. Their work highlights that higher turbulence levels promote earlier transition and larger skin-friction downstream. Morse & Mahesh [8] quantify how the choice of tripping device—resolved wire versus wall-normal blowing—leaves a persistent offset in boundary-layer thickness and turbulence anisotropy along the DARPA SUBOFF hull. However, their work did not pay extra attention to wall pressure fluctuations.

In this work, wall-resolved large-eddy simulations (WRLES) are carried out for flow over the DARPA SUBOFF bare hull at a Reynolds number of $Re_L = 1.1\times10^6$ to systematically assess the effects of different tripping strategies on boundary-layer transition and wall pressure fluctuations. Two representative approaches are examined: a numerical trip implemented via wall-normal blowing and a physical trip wire represented by a localized geometric perturbation. Particular attention is paid to the spatial development of wall pressure fluctuations, including their intensity, downstream evolution, and sensitivity to the tripping method. By comparing the transition behavior and near-wall pressure statistics induced by these two approaches, the present study aims to clarify the extent to which numerical tripping may introduce artificial effects and to provide guidance for selecting appropriate tripping strategies in high-fidelity simulations of axisymmetric underwater vehicle flows.

2. NUNERICAL METHODOLOGY

2.1 Governing equations

Large-eddy simulations (LES) are incapable of resolving vortices of all scales in the flow field. By applying a filter to the incompressible N-S equations, the governing equations for LES can be obtained.

$$\frac{\partial \tilde{u}_i}{\partial x_i} = 0 \tag{1}$$

$$\frac{\partial \tilde{u}_i}{\partial t} + \frac{\partial \tilde{u}_i \tilde{u}_j}{\partial x_j} = -\frac{1}{\rho}\frac{\partial \tilde{p}}{\partial x_i} + \nu \frac{\partial^2 \tilde{u}_i}{\partial x_j \partial x_j} + \frac{\partial \tau_{ij}^{sgs}}{\partial x_j} \tag{2}$$

where $\tilde{u}_i$ (i = 1, 2, 3) is the filtered velocity component in the x_i direction of the flow field, $\tilde{p}$ is the filtered pressure of the flow field, ν is the kinematic viscosity of the fluid and τ_{ij}^{sgs} is the SGS stress term. τ_{ij}^{sgs} is given by

$$\tau_{ij}^{sgs} = 2\nu_{sgs}\tilde{S}_{ij} + \frac{1}{3}\tau_{kk}^{sgs}\delta_{ij} \tag{3}$$

where $\tilde{S}_{ij}$ is the resolved strain-rate tensor, δ_{ij} is the Kronecker delta, ν_{sgs} is the SGS eddy viscosity. In this study, the wall-adapting local eddy-viscosity (WALE) model [11] is applied as

$$\nu_{sgs} = (C_w\Delta)^2 \frac{(S_{ij}^d S_{ij}^d)^{3/2}}{(\tilde{S}_{ij}\tilde{S}_{ij})^{5/2} + (S_{ij}^d S_{ij}^d)^{5/4}} \tag{4}$$

where $C_w = 0.325$ is the WALE coefficient, Δ is the cube root of local cell volume, S_{ij}^d is the traceless symmetric part of the square of the velocity gradient tensor.

2.1 Computational domain and mesh

A schematic of the computational domain is shown in Figure 1. The coordinate system is defined with the origin O located at the nose of the body, where the x-axis is aligned with the incoming flow direction. The inlet boundary is placed $4R$ upstream of the nose, where R denotes the maximum radius of the hull. In the radial direction, the outer boundary is positioned at a distance of $4R$ from the hull surface. Given that the present study mainly focus on the boundary layer transition, the streamwise length of the computational domain only extends to approximately $0.5L$ downstream of the nose, where L is the total length of the body.

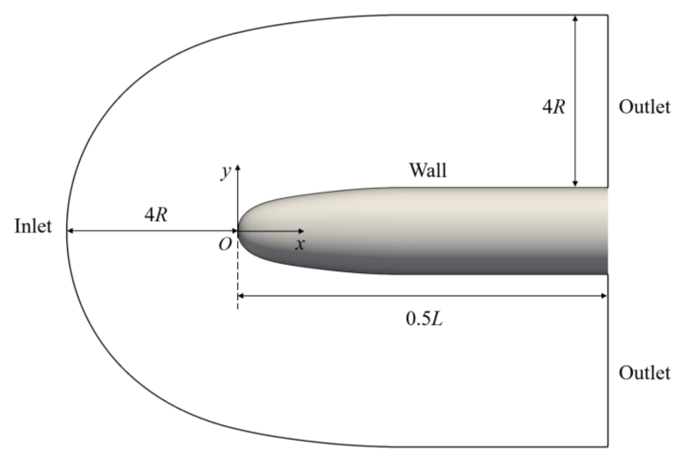

FIGURE 1: COMPUTATIONAL DOMAIN

Figure 2 shows the computational meshes used in present study. A fully structured mesh is employed to discretize the computational domain. Grid refinement is applied in the near-wall region to adequately capture the viscous sublayer and the inner portion of the turbulent boundary layer. The mesh is gradually stretched in the wall-normal direction using a geometric progression, ensuring smooth cell size variation and avoiding abrupt changes in grid spacing. The first wall-normal grid layer satisfies $\Delta y_w^+ < 1$ (where the superscript '+' denotes a non-dimensional parameter scaled by the wall friction velocity u_τ and the viscous length scale ν/u_τ). The near-wall streamwise grid resolution at the mid-body is $\Delta x^+ = 33$ and the azimuthal grid resolution is $r^+\Delta\theta = 11$, which are same with the resolutions used in previous study [5,8]. The total numbers of grids are approximately 130 million and 134 million for numerical trip case and circular trip case, respectively. The time step used in the simulation is $\Delta t^* = \Delta t U_\infty / L = 4.35\times10^{-5}$, ensuring that the Courant-Friedrichs-Lewy number is satisfied with $CFL < 1$. The resulting structured mesh exhibits good orthogonality and low skewness throughout the domain, providing a reliable basis for the WRLES conducted in the present study.

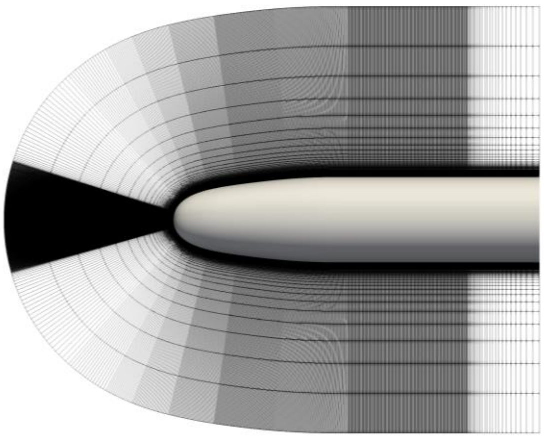

(a) NUMERICAL TRIP

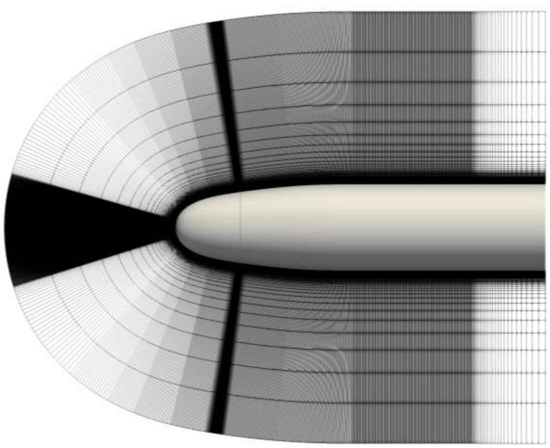

(b) CIRCULAR TRIP

FIGURE 2: GLOBAL VIEW COMPUTATIONAL MESH

To prompt rapid transition to turbulence, artificial transition is introduced at the bow (x/D = 0.75, D denotes the maximum diameter of the hull). The trip location is same as that used in the experiments [3] and the numerical simulations [5]. As shown in Figure 3, special attention is paid to the grid quality in the vicinity of the tripping device. For the circular trip wire case, a localized mesh refinement is introduced around the geometric perturbation to accurately resolve the flow disturbance induced by the trip wire while maintaining overall grid smoothness. The diameter of the obstacle is $0.0075D$. In the numerical tripping case, the grid distribution remains unchanged. Several perturbations with different amplitudes were tested, and a value of $0.18U_\infty$ was found to be the minimum value that satisfied the requirements.

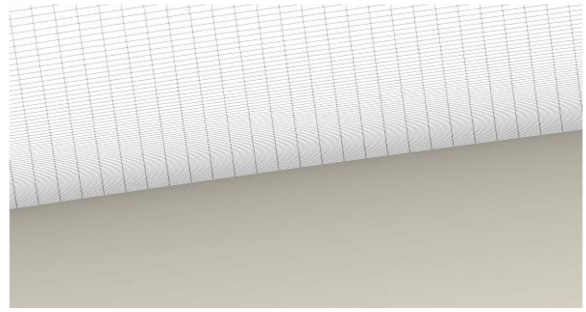

(a) NUMERICAL TRIP

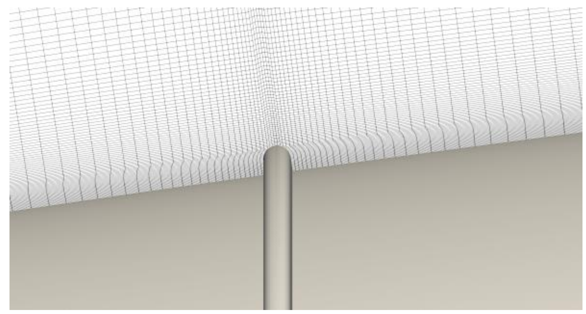

(b) CIRCULAR TRIP

FIGURE 3: COMPUTATIONAL MESH NEAR THE TRIPPING REGION

The present simulation is performed using the open-source CFD platform OpenFOAM. In terms of the numerical schemes and solver, the coupled pressure-velocity is solved using the PISO algorithm [12]. In addition, the temporal term employs the second-order implicit backward scheme [13]. The gradient and Laplacian terms are discretized using the second-order linear scheme. Regarding the discretization of the convective term, the linear upwind stabilized transport (LUST) scheme is used [14,15]. This scheme uses a weighted average of 75% linear central and 25% linear upwind scheme to compute cell-face values, resulting in second-order accuracy.

3. RESULTS AND DISCUSSION

3.1 Validation

Figure 4 presents the streamwise distribution of the surface pressure coefficient C_p along the SUBOFF bare hull, comparing the present numerical results obtained using different tripping strategies with the experimental data [2]. The pressure coefficient is defined as follows:

$$C_p = \frac{p - p_\infty}{0.5\rho U_\infty^2}, \tag{5}$$

where p_∞ represents the reference pressure. Overall, both tripping approaches reproduce the main pressure trends along the hull, including the rapid pressure drop near the nose, the subsequent pressure recovery, and the gradual relaxation toward an approximately constant level in the downstream region.

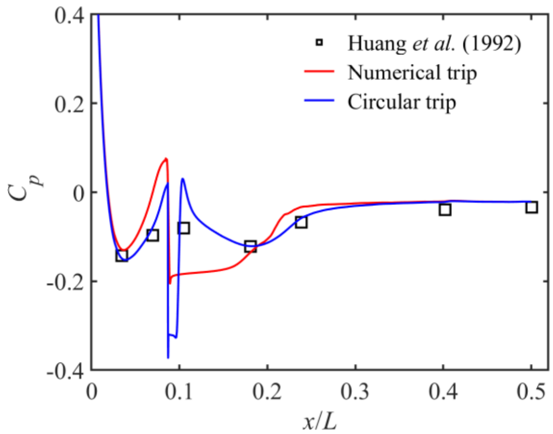

FIGURE 4: MEAN PRESSURE COEFFICIENTS ON THE HULL

In the forebody region ($x/L < 0.2$), pronounced differences are observed between the two tripping methods. The circular trip wire induces a sharp and highly localized disturbance in the pressure distribution, manifested as a strong negative pressure spike immediately downstream of the trip location. This abrupt pressure drop is associated with local flow separation and intense vortical structures generated by the geometric perturbation. However, the pressure recovers rapidly downstream, and the C_p distribution closely realigns with the experimental data beyond the immediate vicinity of the trip.

By contrast, the numerical trip based on wall-normal blowing produces a smoother but more spatially extended modification of the pressure field. The pressure overshoot upstream of the transition location and the delayed recovery indicate a more gradual and less localized transition process. As a result, the numerical trip leads to a sustained deviation from the experimental pressure levels over a broader streamwise extent.

Further downstream ($x/L > 0.2$), the pressure distributions obtained using both tripping strategies converge and show good agreement with the experimental measurements. This convergence indicates that the influence of the tripping method on the mean pressure field diminishes once a fully developed turbulent boundary layer is established. Nevertheless, the discrepancies observed in the forebody region highlight the sensitivity of surface pressure characteristics to the tripping approach, particularly in the vicinity of laminar–turbulent transition.

3.2 Instantaneous flow field

Figure 5 illustrates the instantaneous vortical structures visualized by the iso-surfaces of the Q-criterion at $Q = 500$, colored by the normalized streamwise velocity U_x/U_∞, for the numerical trip and circular trip cases. For the numerical trip case (Fig. 5a), the flow downstream of the trip location is characterized by the emergence of large-scale, streamwise-elongated vortical structures that persist over an extended streamwise distance. These structures appear relatively organized and exhibit strong spatial coherence, indicating a gradual and spatially distributed transition process. The sustained presence of energetic vortices in the near-wall region suggests that the numerical trip introduces a broad disturbance to the boundary layer, leading to an extended transitional regime rather than a sharply localized transition. This behavior is consistent with the smoother but more widespread modification observed in the surface pressure distribution.

In contrast, the circular trip wire case (Fig. 5b) exhibits a markedly different vortical organization. Immediately downstream of the trip wire, intense vortical structures are generated in a highly localized region, forming dense clusters of small-scale vortices associated with strong shear and localized flow separation. These vortices rapidly break down into finer-scale turbulent motions, and the flow transitions quickly to a fully developed turbulent state. The influence of the trip wire is confined primarily to the immediate vicinity of the trip location.

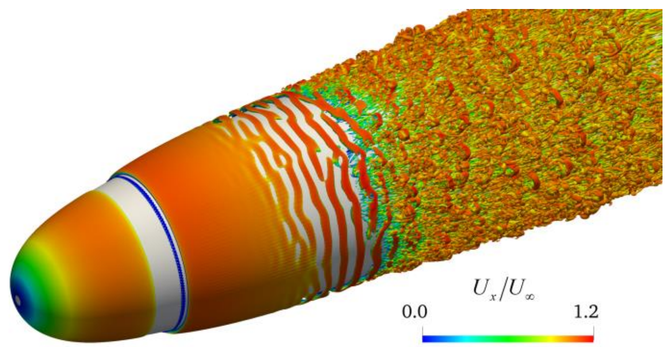

(a) NUMERICAL TRIP

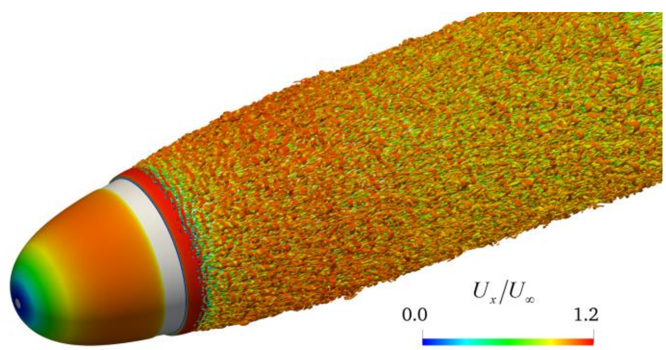

(b) CIRCULAR TRIP

FIGURE 5: INSTANTANEOUS NEAR-WALL VORTICAL STRUCTURES VISUALIZED BY ISO-SURFACES OF THE Q-CRITERION

Figure 6 shows instantaneous contours of the normalized streamwise velocity U_x/U_∞ in the near-wall region, with the black line indicating the boundary-layer edge. The two cases correspond to the numerical trip and the circular trip wire, respectively. For the numerical trip case (Fig. 6a), a large separation bubble is observed downstream of the trip location. Within the separation bubble, velocity fluctuations appear weak and intermittently distributed in the early downstream region, suggesting that the injected wall-normal disturbance promotes transition in a diffuse manner rather than through a sharply localized mechanism. As a result, the boundary layer remains relatively thick over an extended streamwise distance, consistent with the presence of large-scale coherent structures observed in the Q-criterion visualization.

In contrast, the circular trip wire case (Fig. 6b) shows a markedly different instantaneous flow structure. Immediately downstream of the trip wire, intense velocity fluctuations are generated close to the wall, accompanied by a rapid distortion of the boundary-layer edge. The boundary layer thickens abruptly over a short streamwise distance, indicating a prompt transition to turbulence. The near-wall region is populated by fine-scale structures and strong velocity gradients, characteristic of a fully developed turbulent boundary layer. Further downstream, the boundary-layer edge stabilizes and exhibits a more uniform growth, suggesting that the influence of the trip wire is largely confined to the immediate vicinity of the trip location.

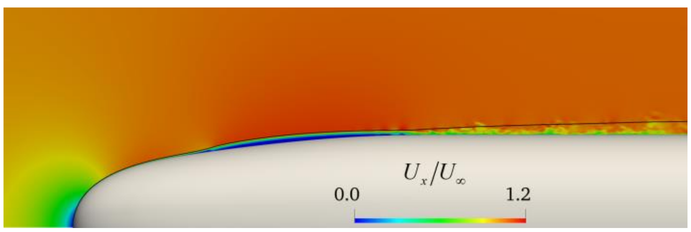

(a) NUMERICAL TRIP

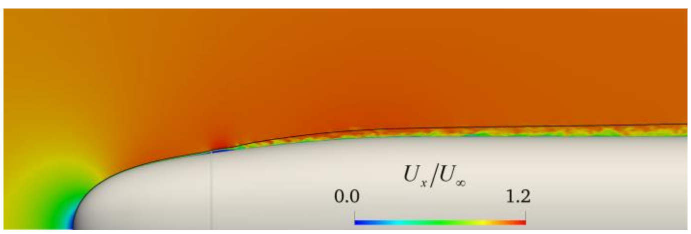

(b) CIRCULAR TRIP

FIGURE 6: INSTANTANEOUS STREAMWISE VELOCITY FIELD

Figure 7 shows instantaneous contours of the pressure field normalized by the free-stream dynamic pressure, p/q_∞, where $q_\infty = 1/2\,\rho U_\infty^2$. For the numerical trip case (Fig. 7a), the pressure field downstream of the trip location exhibits a relatively smooth and spatially extended low-pressure region along the wall. The pressure depression is not sharply localized but instead spreads gradually in the streamwise direction, reflecting a diffuse transition process. Instantaneous pressure fluctuations appear weak and intermittent in the early downstream region, and no pronounced localized pressure extrema are observed near the trip location. This behavior is consistent with the surface pressure coefficient distribution, where the numerical trip produces a smoother but more extended deviation from the experimental data.

In contrast, the circular trip wire case (Fig. 7b) shows a markedly different instantaneous pressure signature. Immediately downstream of the trip wire, a strong and highly localized low-pressure region is observed near the wall, associated with intense shear and localized flow separation induced by the geometric perturbation. This localized pressure deficit corresponds directly to the sharp negative peak in the surface pressure coefficient distribution near the trip location. Further downstream, the pressure field recovers rapidly, and the instantaneous pressure fluctuations become more uniformly distributed within the boundary layer, consistent with the rapid establishment of a fully turbulent boundary layer observed in the velocity and vortical structure visualizations.

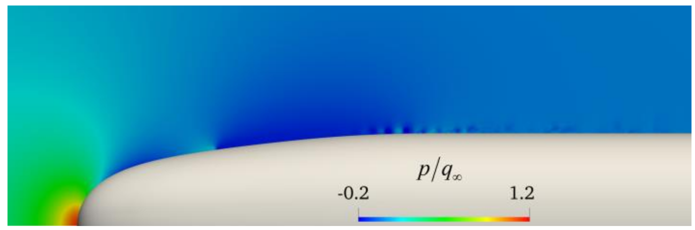

(a) NUMERICAL TRIP

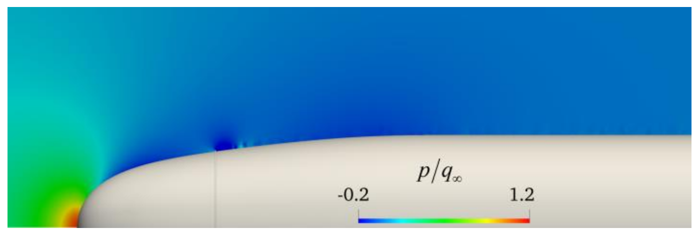

(b) CIRCULAR TRIP

FIGURE 7: INSTANTANEOUS PRESSURE FIELD

3.3 Wall pressure fluctuations

Figure 8 presents instantaneous contours of the wall pressure fluctuations, p'/q_∞, over the forebody region of the SUBOFF bare hull for the numerical trip and circular trip cases. For the numerical trip case (Fig. 8a), the wall pressure fluctuations exhibit a relatively broad and streamwise-elongated distribution downstream of the trip location. The fluctuation patterns appear organized into large-scale, low-wavenumber streaks that persist over an extended streamwise region. Although the peak fluctuation levels are moderate, the spatial extent of the pressure fluctuation field is considerable, indicating that unsteady pressure activity is sustained over a long transitional region. This behavior is consistent with the diffuse transition process observed in the instantaneous velocity and pressure fields, as well as with the presence of large-scale coherent vortices identified using the Q-criterion. The numerical trip therefore induces a widespread modulation of wall pressure fluctuations rather than a sharply localized response.

In contrast, the circular trip wire case (Fig. 8b) shows a markedly different instantaneous wall pressure fluctuation pattern. Strong pressure fluctuations are concentrated immediately downstream of the trip wire, forming a narrow circumferential band of intense alternating pressure peaks and troughs. These localized high-amplitude fluctuations are associated with the strong shear layers and vortical structures generated by the geometric perturbation. Downstream of this region, the pressure fluctuation field rapidly becomes more spatially homogeneous, with smaller-scale and more uniformly distributed fluctuations characteristic of a fully developed turbulent boundary layer.

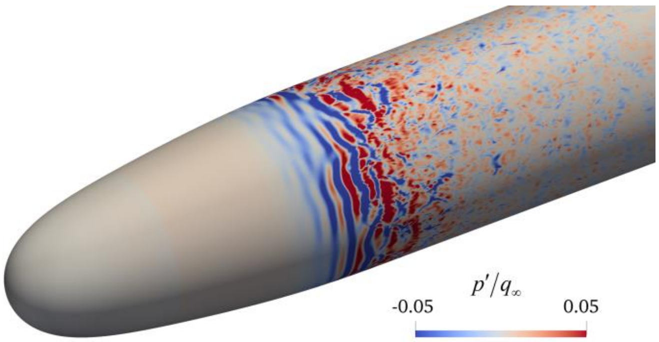

(a) NUMERICAL TRIP

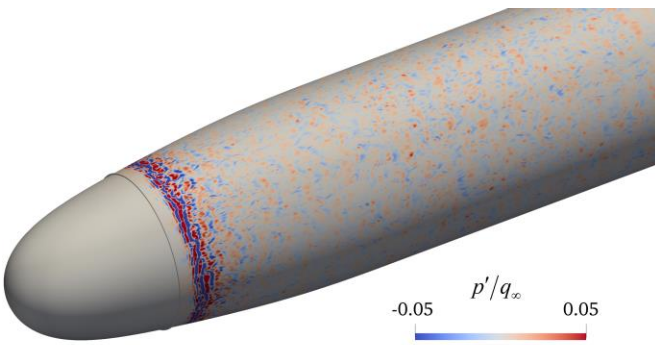

(b) CIRCULAR TRIP

FIGURE 8: INSTANTANEOUS FLUCTUATING WALL PRESSURE FIELD

Figure 9 shows the distribution of the root-mean-square wall pressure fluctuations, $p_{w,rms}/q_\infty$, over the forebody of the SUBOFF bare hull for the numerical trip and circular trip cases. The RMS field provides a statistical measure of the cumulative unsteady pressure activity at the wall and highlights the integrated effect of the transition process induced by different tripping strategies. For the numerical trip case (Fig. 9a), elevated wall pressure RMS levels are observed over a relatively broad streamwise region downstream of the trip location. The region of enhanced $p_{w,rms}$ extends gradually along the hull, forming a wide band of moderate fluctuation intensity. Although the peak RMS values are not excessively large, the spatial extent of elevated pressure fluctuations is significant, indicating that unsteady pressure activity persists over an extended transitional region. This behavior is consistent with the diffuse transition process identified in the instantaneous velocity and pressure fields, as well as with the large-scale, streamwise-coherent vortical structures observed in the *Q*-criterion visualization. The numerical trip therefore leads to a sustained amplification of wall pressure fluctuations over a long streamwise distance.

In contrast, the circular trip wire case (Fig. 9b) exhibits a sharply localized region of very high wall pressure RMS immediately downstream of the trip wire. The peak $p_{w,rms}$ values are significantly higher than those observed in the numerical trip case, forming a narrow circumferential band associated with the intense shear layers and strong vortical motions generated by the geometric perturbation. However, this high-intensity region decays rapidly in the downstream direction. Beyond the immediate vicinity of the trip wire, the wall pressure RMS levels decrease quickly and become relatively uniform along the hull, indicating the establishment of a fully developed turbulent boundary layer with statistically homogeneous pressure fluctuations.

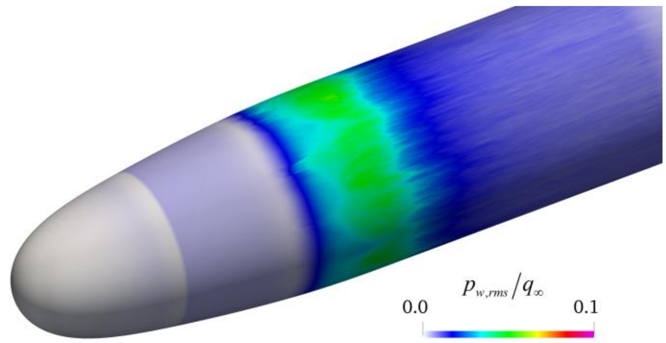

(a) NUMERICAL TRIP

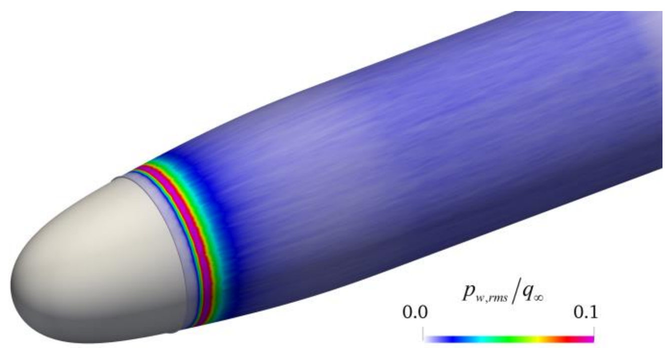

(b) CIRCULAR TRIP

FIGURE 9: ROOT-MEAN-SQUARE WALL PRESSURE FLUCTUATIONS

4. CONCLUSIONS

In this study, wall-resolved large-eddy simulations were conducted for flow over the DARPA SUBOFF bare hull at $Re_L = 1.1\times10^6$ to investigate the effects of different tripping strategies on boundary-layer transition and wall pressure fluctuations. Two representative approaches were examined: a numerical trip implemented via wall-normal blowing and a physical circular trip wire modeled as a localized geometric perturbation. The main conclusions are summarized as follows.

Firstly, the two tripping strategies lead to fundamentally different transition mechanisms. The numerical trip induces a smoother but more spatially extended transition process, characterized by gradual boundary-layer thickening and a prolonged transitional region. In contrast, the circular trip wire triggers a rapid and highly localized transition, producing an abrupt boundary-layer thickening and a quick establishment of a fully developed turbulent boundary layer.

Secondly, the statistical analysis of wall pressure fluctuations highlights the contrasting impact of the two tripping strategies. The numerical trip yields moderate peak RMS levels but sustains elevated wall pressure fluctuations over an extended region, indicative of an over-tripping effect. In contrast, the circular trip wire produces significantly higher RMS levels in a narrow circumferential band near the trip location, followed by rapid downstream homogenization consistent with physically realistic turbulent boundary-layer development.

Overall, the present results demonstrate that the choice of tripping strategy plays a critical role in shaping both the transition process and the resulting wall pressure fluctuations. While numerical tripping via wall-normal blowing is convenient to implement, it may introduce artificial, spatially extended pressure-fluctuation effects. The circular trip wire, on the other hand, provides a more realistic and localized representation of transition-induced pressure dynamics for high-Reynolds-number axisymmetric boundary layers. These findings offer useful guidance for the selection and implementation of tripping methods in high-fidelity simulations of underwater vehicle flows, particularly when accurate prediction of wall pressure fluctuations is required.

ACKNOWLEDGEMENTS

This work was supported by the National Natural Science Foundation of China (51909160, 52131102) and the National Key Research and Development Program of China (2022YFC2806705).

REFERENCES

[1] N. C. Groves, T. T. Huang, and M. S. Chang, *Geometric Characteristics of DARPA SUBOFF Models: (DTRC Model Nos. 5470 and 5471)* (David Taylor Research Center, 1989).

[2] T. Huang, H. L. Liu, N. C. Groves, T. Forlini, J. Blanton, and S. Gowing, *Measurements of Flows over an Axisymmetric Body with Various Appendages in a Wind Tunnel: The DARPA SUBOFF Experimental Program*, in *Proceedings of the 19th Symposium on Naval Hydrodynamics* (National Academy Press, Seoul, Korea, 1992).

[3] J. M. Jiménez, M. Hultmark, and A. J. Smits, The intermediate wake of a body of revolution at high Reynolds numbers, J. Fluid Mech. **659**, 516 (2010).

[4] J. M. Jiménez, R. T. Reynolds, and A. J. Smits, The effects of fins on the intermediate wake of a submarine model, J. Fluids Eng. **132**, (2010).

[5] P. Kumar and K. Mahesh, Large-eddy simulation of flow over an axisymmetric body of revolution, J. Fluid Mech. **853**, 537 (2018).

[6] A. Posa and E. Balaras, A numerical investigation about the effects of Reynolds number on the flow around an appended axisymmetric body of revolution, J. Fluid Mech. **884**, A41 (2020).

[7] N. Morse and K. Mahesh, Large-eddy simulation and streamline coordinate analysis of flow over an axisymmetric hull, J. Fluid Mech. **926**, A18 (2021).

[8] N. Morse and K. Mahesh, Tripping effects on model-scale studies of flow over the DARPA SUBOFF, J. Fluid Mech. **975**, A3 (2023).

[9] G. Q. Fan, H. Chen, W. W. Zhao, and D. C. Wan, Scaling laws and space–time characteristics of wall pressure fluctuations in an axisymmetric boundary layer with varying pressure gradient, J. Fluid Mech. **1016**, A28 (2025).

[10] F. Zhu, J. W. Jiang, C. X. Xu, and W. X. Huang, Numerical study on boundary layer flow over the bow of SUBOFF model with turbulent inflow, J. Fluid Mech. **1023**, A10 (2025).

[11] F. Nicoud and F. Ducros, Subgrid-scale stress modelling based on the square of the velocity gradient tensor, Flow Turbul. Combust. **62**, 183 (1999).

[12] R. I. Issa, Solution of the implicitly discretised fluid flow equations by operator-splitting, J. Comput. Phys. **62**, 40 (1986).

[13] H. Jasak, Error Analysis and Estimation for the Finite Volume Method with Applications to Fluid Flows, PhD thesis, Imperial College, University of London, 1996.

[14] H. Weller, Controlling the computational modes of the arbitrarily structured C grid, Mon. Weather Rev. **140**, 3220 (2012).

[15] J. Martínez, F. Piscaglia, A. Montorfano, A. Onorati, and S. M. Aithal, Influence of spatial discretization schemes on accuracy of explicit LES: canonical problems to engine-like geometries, Comput. Fluids **117**, 62 (2015).